Available online at www.sciencedirect.com
ScienceDirect
Acta Materialia 57 (2009) 2362–2375
Acta MATERIALIA
www.elsevier.com/locate/actamat

# Load partitioning in $Al_2O_3$–Al composites with three-dimensional periodic architecture

M.L. Young [a,*], R. Rao [c], J.D. Almer [b], D.R. Haeffner [b], J.A. Lewis [c], D.C. Dunand [a]

[a] Department of Materials Science and Engineering, Northwestern University, Evanston, IL 60208, USA
[b] Advanced Photon Source, Argonne National Laboratory, Argonne, IL 60439, USA
[c] Department of Materials Science and Engineering, University of Illinois at Urbana-Champaign, IL 61801, USA

Received 2 October 2008; received in revised form 12 January 2009; accepted 15 January 2009
Available online 5 March 2009

**Abstract**

Interpenetrating composites are created by infiltration of liquid aluminum into three-dimensional (3-D) periodic $Al_2O_3$ preforms with simple tetragonal symmetry produced by direct-write assembly. Volume-averaged lattice strains in the $Al_2O_3$ phase of the composite are measured by synchrotron X-ray diffraction for various uniaxial compression stresses up to −350 MPa. Load transfer, found by diffraction to occur from the metal phase to the ceramic phase, is in general agreement with simple rule-of-mixture models and in better agreement with more complex, 3-D finite-element models that account for metal plasticity and details of the geometry of both phases. Spatially resolved diffraction measurements show variations in load transfer at two different positions within the composite.


*Keywords:* Metal matrix composites (MMC); Synchrotron radiation; X-ray diffraction (XRD); Aluminum; Compression test

## 1. Introduction

Interpenetrating phase composites (IPCs) are characterized by two co-continuous and percolating phases [1]. Ceramic–metal IPCs typically exhibit much higher toughness than pure ceramics. Several liquid-metal processing routes exist for creating $Al_2O_3$–Al IPCs, including infiltration of porous $Al_2O_3$ preforms [2–6], reactive metal penetration [7,8] and infiltration with displacement reactions [9,10]. These processes typically lead to a random, isotropic, spatial distribution of the $Al_2O_3$ and Al phases within the composite. Recently, $Al_2O_3$–Al IPCs with a highly regular architecture and tailored properties were created by infiltrating liquid aluminum into alumina preforms with three-dimensional (3-D) periodic architectures [11], produced by robocasting, a robotically controlled layerwise deposition of colloidal inks. This method can create structures with spanning (unsupported) features [12–14] and is related to other direct-write techniques, such as ink-jet printing [15] and micro-pen writing [16]. Similarly, mullite–aluminum and alumina–aluminum IPCs were produced by liquid-metal infiltration of mullite or silica preforms created by the fused deposition method [17,18].

In the present paper, we investigate interpenetrating $Al_2O_3$–Al IPCs produced by liquid-metal infiltration of 3-D periodic $Al_2O_3$ preforms with simple tetragonal (ST) symmetry assembled by direct ink writing and previously demonstrated to exhibit an attractive combination of low density, high compressive strength and low thermal expansion, together with expected reasonable toughness and good thermal conductivity [11]. Here, these $Al_2O_3$–Al IPCs are subjected to uniaxial compressive loading, while internal elastic strains are measured by synchrotron X-ray diffraction of the $Al_2O_3$ phase, from which load transfer from the compliant Al phase to stiffer $Al_2O_3$ phase is determined. Simplified analytical models (based on rule-of-mixture considerations) and more realistic 3-D finite-element

* Corresponding author. Tel.: +49 176 24894769; fax: +49 234 3214235.
*E-mail address:* marcus.young@rub.de (M.L. Young).

1359-6454/$36.00 
doi:10.1016/j.actamat.2009.01.019

models are compared with the experimental data, providing insights for the optimal design of IPCs for structural applications.

## 2. Experimental procedure

### 2.1. Materials

Ceramic preforms with a regular 0/90° architecture are produced by direct-write assembly of a colloidal gel-based ink composed of a mixture of 95 vol.% $Al_2O_3$–5 vol.% $ZrO_2$ particles suspended in water with a total solids content of ~52 vol.%. Fig. 1 provides an idealized schematic of the 3-D sintered preforms with ST symmetry. The preforms are assembled in a layerwise sequence via direct writing. The first layer consists of parallel array of ink filaments (or rods), while the subsequent layer consists of parallel rods oriented in the orthogonal direction. "Hairpins" connect each filament in the horizontal (2–3) planes. This two-layer pattern is repeated 15 times to create the desired 30-layer preform. After fabrication, these preforms are dried in air for 24 h and then sintered in air at 1600 °C for 2.5 h, resulting in a final rod diameter of approximately 250 μm in the densified structures with nominal preform dimensions of $5 \times 5 \times 10$ mm$^3$. Additional details for the ink design and fabrication process are provided in Refs. [11,19].

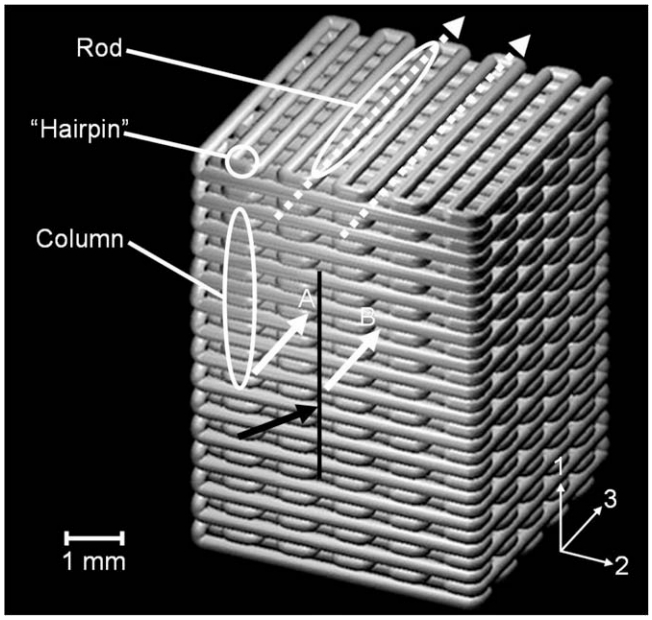


Fig. 1. Idealized schematic of 3-D ceramic preform with ST symmetry. The metal phase (not shown) fills the space between the ceramic rods (diameter ~250 μm) and forms a skin (~100 μm deep) around the preform. The black arrow forming a 22° angle with the face corresponds to the beam used for 3 mm measurements, with the area rastered shown as the black line. The two white arrows perpendicular to the face show the X-ray beam ($150 \times 150$ μm$^2$) for spatially resolved measurements at positions (A) and (B). The corresponding beam path is illustrated with dashed line at the top of the preform, showing that position (A) samples a ceramic rod (consisting of both column and span regions) while position (B) samples a single ceramic hairpin (as well as metal).

Sintered ceramic preforms are centered within cuboidal cavities machined into a graphite block with dimensions larger by ~1 mm than an individual preform. The graphite block is placed within a graphite crucible and a billet of either 99.99% pure Al or 7075-Al alloy (Al–5.6Zn–2.5Mg–1.6Cu–0.23Cr, in wt.%) is placed on top of the graphite. The crucible is introduced in a gas-pressure, liquid-metal infiltration apparatus [20] and heated under vacuum to a temperature of 750 °C. The liquid metal is infiltrated into the evacuated open volume of the preform under an argon pressure of 3.5 MPa and the resulting composite is directionally solidified. For one smaller specimen ($4.51 \times 4.52 \times 9.74$ mm$^3$), all excess metal is removed from the outer faces of the sample, leaving the edges of the ceramic preform exposed. Two larger specimens ($5.22 \times 5.27 \times 9.94$ mm$^3$) are machined so that a ~0.5 mm thick metal outer layer remains around the ceramic preform, which is thus not exposed. The pure Al composites are annealed for 2 h at 350 °C and air cooled. The 7075 alloy composites are annealed for 1 h at 490 °C, water quenched, annealed for 24 h at 120 °C, and then water quenched again, corresponding to a T6 heat-treatment.

### 2.2. Synchrotron diffraction measurements

Similar to the experimental setup in Refs. [21–28], high-energy X-ray diffraction measurements are collected at the 1-ID and 11-ID beam lines of the Advanced Photon Source (Argonne National Laboratory, IL) using a monochromatic 81 keV ($\lambda = 0.015$ nm) or 93 keV ($\lambda = 0.013$ nm) X-ray beam for 60 s. The incident X-ray beam in diffraction mode generally had a square cross-section with a size of $150 \times 150$ μm$^2$. Complete Debye–Scherrer diffraction rings from the crystalline phases present in the diffraction volumes are recorded using an image plate (MAR345) with 345 mm diameter, providing a 100 μm pixel size with a 16 bit dynamic range. The sample-to-camera distance was 1.220 or 2.100 m. A typical diffraction pattern for the latter sample-to-camera distance is shown in Fig. 2. While use of the longer diffraction distance provides information about fewer diffraction rings, such as the loss of the (300) reflection, better resolution in strain measurements is achieved. Additional calibration diffraction cones are produced from a paste composed of vacuum grease and pure ceria ($CeO_2$) powder, which is smoothly applied to the back surface of the composite. As illustrated in Fig. 2, all phases present are fine-grained and polycrystalline, leading to smooth diffraction rings, except for the Al phase, which is coarse-grained (due to the casting method) and thus produces spotty diffraction rings that cannot be used for strain measurements. As described in detail in Ref. [27], the programs FIT2D [29,30] and MATLAB [31] are used to determine lattice strains from distortions of the diffraction rings of the $Al_2O_3$ and $ZrO_2$ phases. The $CeO_2$ reflections near the center (111) and (200) and outer edge (220) of the detector, respectively, are used for calibration purposes.

The two larger composites with an Al outer layer (labeled S-Al for pure Al and S-7075 for the alloyed com-

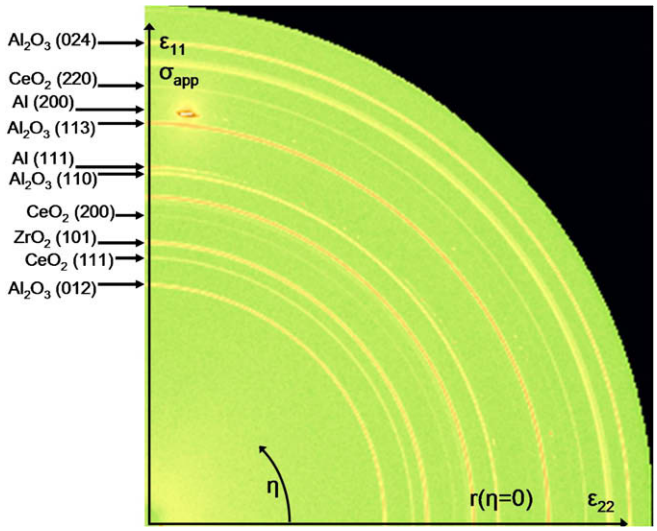


Fig. 2. Representative X-ray diffraction pattern (quarter of image plate) of composite S-Al for an average bulk measurement. All full diffraction rings were identified and assigned to $CeO_2$, $Al_2O_3$ or $ZrO_2$, while the Al rings were spotty and incomplete. For clarity, only some of the rings are labeled here. The sample-to-camera distance for this diffraction pattern was 2.100 m. Strains $\varepsilon_{11}$ and $\varepsilon_{22}$ are measured in the direction shown.

posites, where "S" stands for "simple tetragonal") are subjected to uniaxial compressive loading and unloading with ~15 MPa stress increments. The third, smaller specimen without Al outer layer (labeled S-Al(R), where "R" stands for "spatially resolved") is used to carry out spatially resolved measurements. These in situ uniaxial compressive experiments are performed using a small, custom-built, screw-driven loading system in a general setup described in more detail previously [19,21–28,32]. Synchrotron X-ray diffraction measurements are collected at each stress level. For average bulk measurements, the horizontal beam impinges on the vertical composite face at a 22° angle and strain measurements are collected during a vertical 3 mm raster near the center of the composite. The total diffracting volume is about 1.6 $mm^3$ (Fig. 1). For spatially resolved measurements, the composite is positioned with one of its vertical faces perpendicular to the horizontal beam (Fig. 1). Two positions (A and B) are studied, as shown in Figs. 1 and 3: (i) along a horizontal ceramic rod (A); and (ii) between ceramic rods, along a metallic horizontal channel (B). Since the beam width (150 μm) is smaller than the ceramic rod width (~250 μm), the beam path along the ceramic rod for position (A) consists of roughly equal fractions of ceramic "columns" and "struts"; in position (B), the only ceramic volume diffracting is the "hairpin" connecting two adjacent horizontal rods.

## 3. Results

### 3.1. Microstructure

The ceramic volume fractions of the three composites range from 50% to 60%, as determined from density measurements by He pycnometry. Variations in densities are due to different amounts of pure Al in the outer layer of the composite. Dimensions cannot be used for density evaluation, due to slight edge rounding. In Ref. [11], a similar but smaller composite (nominal dimensions: $4 \times 4 \times 6$ $mm^3$ with a 0.5 mm Al "skin") is reported to have a ceramic volume fraction of 70 vol.%, which is higher than the average ceramic fraction of 53 vol.% for S-Al and S-7075 with outer Al layers. This discrepancy may be explained by our use of an experimentally measured density for $Al_2O_3$–5 vol.% $ZrO_2$ of $4.075 \pm 0.008$ g/$cm^3$. This value is significantly higher than that used in Ref. [11] (3.7 g $cm^{-3}$) and is much closer to the theoretical value of 4.07 g $cm^{-3}$ estimated in Ref. [11]. The lower density used in Ref. [11] was due to porosity within the ceramic of up to 9%, whereas the present preforms were not porous due to improved preform fabrication.

As illustrated in Fig. 3, an X-ray phase-enhanced radiograph shows good alignment of the layers and good spacing between horizontal columns except near the sample edges. No large-scale porosity is observed, as expected from the above density measurements.

### 3.2. Synchrotron diffraction strain measurements

#### 3.2.1. Commonality among samples

For all three samples, plots of the applied stress vs. average elastic lattice strain for the $Al_2O_3$ (1 1 3) or (3 0 0) reflection are shown in Figs. 4–7. Several other $Al_2O_3$ reflections were used to calculate lattice strains but are not shown, since the above two reflections are representative of the bulk due to the observed nearly isotropic $Al_2O_3$ elastic behavior, as further discussed later when comparing $Al_2O_3$ (1 1 0), (1 1 3), (0 1 2) and (0 2 4) reflections. Similarly, the applied stress vs. average elastic lattice strain for the $ZrO_2$ (1 0 1) reflection (Fig. 4b) is shown for sample S-Al only, since the $ZrO_2$ behavior follows that of the $Al_2O_3$ (1 1 3) reflection and thus does not provide additional information. The only difference is that the stress–strain slope for $ZrO_2$ is lower than that for $Al_2O_3$, as expected theoretically from the respective moduli for pure $Al_2O_3$ ($E_{Al2O3} = 380$ GPa [33]) and pure, partially stabilized $ZrO_2$ ($E_{ZrO2} = 205$ GPa [33]).

In Figs. 4–7 the lattice strains for both the $Al_2O_3$ and $ZrO_2$ phases become more compressive (negative) in the loading direction ($\varepsilon_{11}$) and more tensile (positive) in the transverse direction ($\varepsilon_{22}$), as expected from the uniaxial compressive load applied to the sample in the 1 direction (Fig. 1). Small, varying amounts of residual strains at zero applied stress are observed, and they are invariably tensile in the loading direction and compressive in the transverse direction. Finally, no large-scale damage is evident within the composites, either by direct observation of the sample or from large deviations from linearity in the internal lattice strain vs. applied stress lines during cyclic loading (very small deviations are observed). The following sections discuss in detail the different composites tested and their behavior during compression testing and cyclic loading.

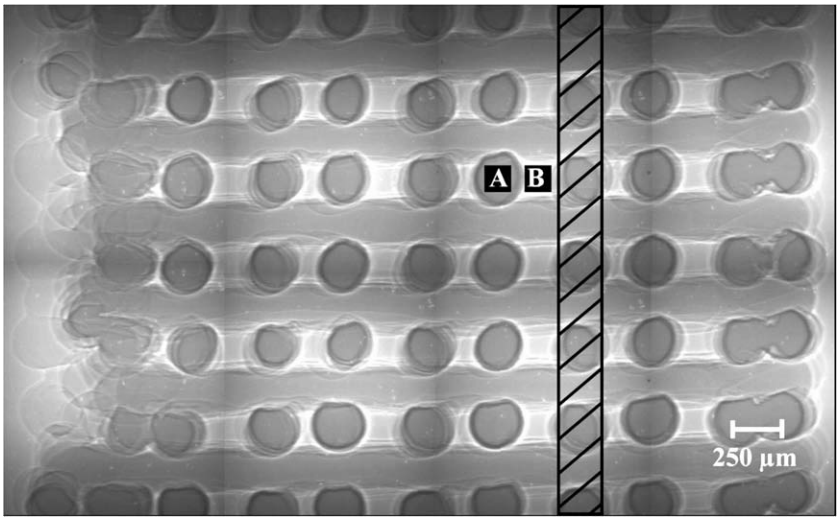


Fig. 3. X-ray phase-enhanced radiograph of middle section of ceramic preform with ST symmetry (projection perpendicular to the 3 direction). The rod diameter is about 250 μm. The black boxes indicate the beam size (150 × 150 μm$^2$) and position of spatially resolved measurements for positions (A) along a ceramic rod and (B) between two rods, the sampling metal phase and a single ceramic "hairpin" connecting two adjacent rods at the edge of the composite. A column, consisting of the overlap in the 1 direction of the perpendicular rods, is highlighted.

*3.2.2. Bulk diffraction measurements*

Sample S-Al, with a density of 3.390 ± 0.003 g cm$^{-3}$ (corresponding to a pure aluminum volume fraction of 49.99 ± 0.24%) and dimensions 5.23 × 5.31 × 9.89 mm$^3$, was cyclically tested without failure as follows: 0 → −66 → −31 MPa, −31 → −129 → −34 MPa, −34 → −196 → −33 MPa and −33 → −322 → 0 MPa. The applied stress vs. average elastic lattice strain for the $Al_2O_3$ (1 1 3) and the $ZrO_2$ (1 0 1) reflections are shown in Fig. 4a and b, respectively.

Before loading, residual strains for the $Al_2O_3$ (1 1 3) reflection are zero within measurement errors (12 με in the loading direction and −12 με in the transverse direction). Upon cyclic elastic loading, the slopes of the $Al_2O_3$ (1 1 3) reinforcement are 242 GPa in the loading direction and 387 GPa in the transverse direction, and remain near-constant as the maximum stress value of the cycle increases.

A similar behavior is observed for the $ZrO_2$ (1 0 1) reflection, as shown in Fig. 4b. Residual strains are again near-zero (44 με in the loading direction and −40 με in the transverse direction). Upon cyclic elastic loading, the slopes of the $ZrO_2$ (1 0 1) phase within the ceramic reinforcement are 156 GPa in the loading direction and 237 GPa in the transverse direction. The maximum longitudinal strain in the $ZrO_2$ phase is 60% higher than in the $Al_2O_3$ phase.

In Fig. 5, the applied stress vs. elastic lattice strains for the $Al_2O_3$ (1 1 0), (1 1 3), (0 1 2) and (0 2 4) reflections show nearly isotropic behavior in $Al_2O_3$, with slopes in the loading direction of 254, 242, 216 and 232 GPa, respectively. The $Al_2O_3$ (1 1 0) reflection is 5–18% stiffer than the $Al_2O_3$ (1 1 3), (0 1 2), and (0 2 4) reflections and the (0 1 2) and (0 2 4) reflections show almost identical behavior which is expected since they are symmetrically equivalent. These two $Al_2O_3$ reflections ((0 1 2) and (0 2 4)) provide an internal check and show the error inherent in strain measurements.

Sample S-7075, with a density of 3.482 ± 0.005 g cm$^{-3}$ (corresponding to a 7075 alloy volume fraction of 43.29 ± 0.40%) and dimensions 5.20 × 5.20 × 9.99 mm$^3$, was cyclically tested without failure as follows: 0 → −134 → −97 MPa, −97 → −201 → −85 MPa, −85 → −266 → −95 MPa, and −95 → −330 → 0 MPa. As illustrated in Fig. 6, residual strains at zero applied stress are tensile in the loading direction (131 με) and compressive in the transverse direction (−93 με) for the $Al_2O_3$ (1 1 3) reflection, thus, shifting the initial starting points for the loading curves. Upon cyclic elastic loading, the slopes of the $Al_2O_3$ (1 1 3) reinforcement are 263 and 443 GPa in the loading and transverse directions, respectively.

*3.2.3. Spatially resolved diffraction measurements*

Sample S-Al(R), with a density of 3.528 ± 0.0027 g cm$^{-3}$ (corresponding to a pure aluminum volume fraction of 39.9 ± 2.0%) and dimensions 4.51 × 4.52 × 9.74 mm$^3$, was tested without failure in a single compressive cycle as follows: −23 → −187 → −34 MPa. At each load increment of ~30 MPa, spatially resolved measurements were taken in two positions along a horizontal rod (marked A in Figs. 1 and 3) and at a "hairpin" connecting two rods (B in Figs. 1 and 3). The resulting applied stress vs. average elastic lattice strain curve for the $Al_2O_3$ (3 0 0) reflection is shown in Fig. 7.

Similar to bulk measurements, residual strains are present for both positions A and B. Since this particular set of data has no value collected at zero applied load, the residual strain is extrapolated based on the slope of the best linear fit of the low-stress region (0–23 MPa). Like the bulk measurements, position A (along a rod) has residual strains at zero applied load which are tensile in the loading direction (136 με) and compressive in the transverse direction (−103 με). However, position B ("hairpin" only) shows a

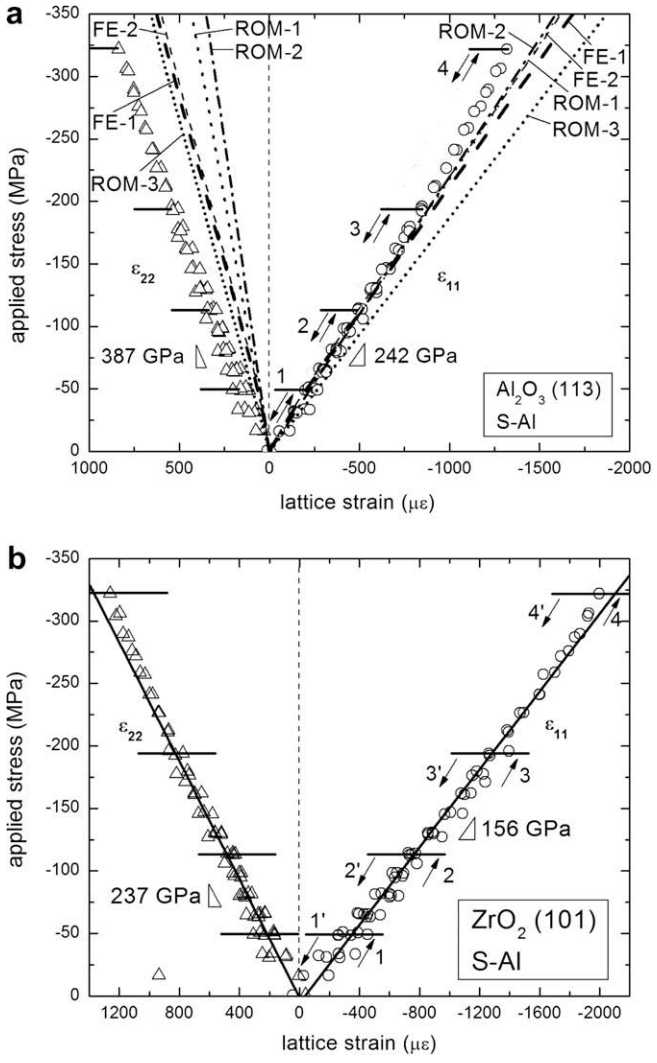


Fig. 4. Applied stress as a function of elastic lattice strain (bulk average values, $\varepsilon_{11}$ parallel and $\varepsilon_{22}$ perpendicular to the applied stress) for S-Al composite using (a) $Al_2O_3$ (113) reflection and (b) $ZrO_2$ (101) upon multiple loading–unloading cycles (marked 1–4). Slopes are best-fit values for all experimental data. Error bars (too small to be represented) are in the range 10–30 με Three rule-of-mixture models (ROM-1, ROM-2 and ROM-3) and two finite-element models (FE-1 and FE-2) for the $Al_2O_3$ phase are also plotted for the two directions.

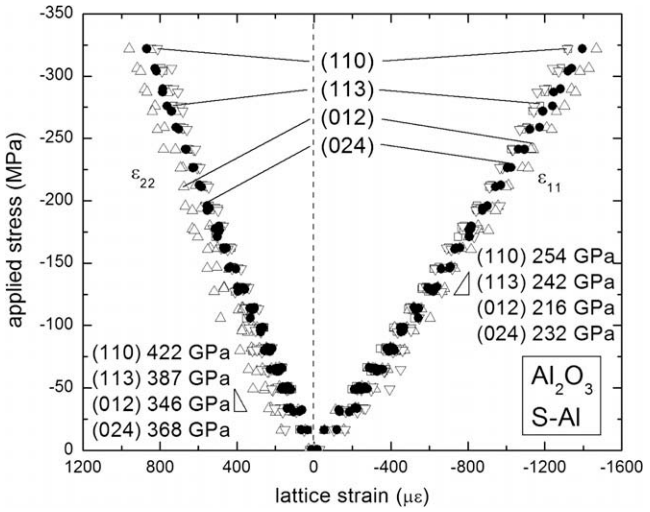


Fig. 5. Applied stress as a function of elastic lattice strain (bulk average values, $\varepsilon_{11}$ parallel and $\varepsilon_{22}$ perpendicular to the applied stress) for S-Al using $Al_2O_3$ (110), (113), (012) and (024) reflections upon multiple loading–unloading cycles. (Although not marked here for clarity, the same four loading steps apply as in Fig. 6a and b.) Slopes are best-fit values for all experimental data. Error bars (too small to be represented) are in the range 10–20 με.

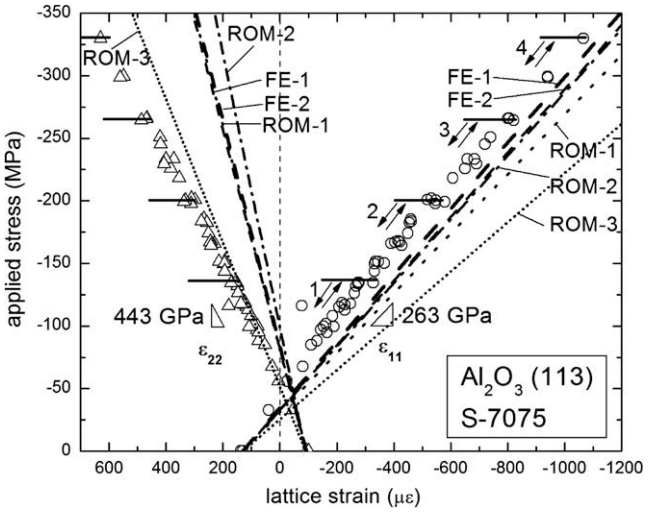


Fig. 6. Applied stress as a function of elastic lattice strain (bulk average values, $\varepsilon_{11}$ parallel and $\varepsilon_{22}$ perpendicular to the applied stress) for S-7075 composite using the $Al_2O_3$ (113) reflection upon multiple loading–unloading cycles (marked 1–4). Slopes are best-fit values for all experimental data. Error bars (too small to be represented) are in the range 10–20 με. Three rule-of-mixture models (ROM-1, ROM-2 and ROM-3) and two finite-element models (FE-1 and FE-2) are also plotted for the two directions.

different behavior, with residual strains which are compressive in the loading direction (−143 με) and tensile in the transverse direction (127 με).

For position A, the slopes of the $Al_2O_3$ (300) reinforcement are 202 GPa in the loading direction and 292 GPa in the transverse direction upon loading. These slopes for position A are lower than the slopes of the bulk measurements (263 GPa in the loading direction and 443 GPa in the transverse direction) by a factor of 0.77 and 0.66. For position B, the slopes of the $Al_2O_3$ (300) reinforcement are 329 GPa in the loading direction and 610 GPa in the transverse direction upon loading, which are higher than the slopes of the bulk measurements by a factor of 1.25 and 1.38.

## 4. Discussion

### 4.1. Bulk measurements

Despite a large mismatch in coefficient of thermal expansion between the two phases ($24.8 \times 10^{-6}\,K^{-1}$ for Al vs. $6.2 \times 10^{-6}\,K^{-1}$ for $Al_2O_3$, at ambient temperature [34,35]), residual strains are near-zero in sample S-Al. This

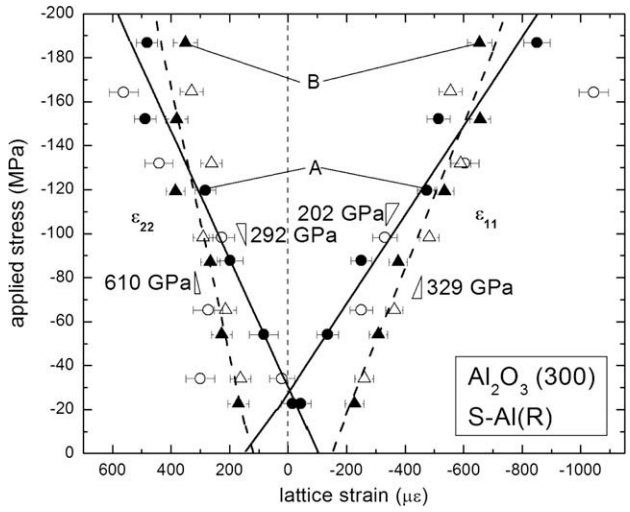


Fig. 7. Applied stress as a function of elastic lattice strain ($\varepsilon_{11}$ parallel and $\varepsilon_{22}$ perpendicular to the applied stress) for S-Al(R) using the $Al_2O_3$ (300) reflection upon loading (closed symbols) and unloading (open symbols). Spatially resolved measurements are along a ceramic rod (A) and along a metallic channel and a single "hairpin" connecting two rods (B). The lines are a linear fit to both loading and unloading data.

can be explained by the slow air-cooling used after annealing and the very low yield stress of 99.99% Al allowing for creep and plastic relaxation of the metal phase. The larger residual strains in sample S-7075 are explained by the water quenching used at the end of the heat-treatment and the higher yield and creep resistance of the metallic phase.

For bulk lattice strain measurements, the stress–strain slopes of the average bulk $Al_2O_3$ (1 1 3) reinforcement phase for S-Al (220–250 GPa, Fig. 5a) and S-7075 composites (240–270 GPa; although not shown here, values were determined from a similar plot to that of Fig. 5a) are approximately 50–60% lower than the Young's modulus for the bulk $Al_2O_3$–5% $ZrO_2$ phase of 365 GPa, as calculated using simple rule-of-mixtures from the moduli of pure $Al_2O_3$ ($E_{Al2O3} = 380$ GPa [33]) and pure, partially stabilized $ZrO_2$ ($E_{ZrO2} = 205$ GPa [33]) This is because load transfer is taking place from the compliant metallic phase to the stiffer ceramic reinforcement and indicates that the stress carried by the $Al_2O_3/ZrO_2$ phase is higher than the applied stress, as observed in many other metal–ceramic composites [36,37]. The metallic phase, however, carries some load, as modeled later, resulting in a higher strength for the composites as compared to uninfiltrated ceramic preforms [11]. The metallic phase further prevents buckling of the ceramic rods and blunts cracks from occurring during failure of the ceramic phase, thus delaying catastrophic failure in compression [11,38–42]. The average stress state of the $Al_2O_3$ phase is far from uniaxial compressive, with ratios of the longitudinal and transverse slopes ranging from 0.59 to 0.63, almost twice the Poisson's ratios value of 0.33 [43] for pure $Al_2O_3$. Similarly, the average stress state of the $ZrO_2$ phase is also far from uniaxial compressive, with a slope ratio of 0.66, which is approximately three times the Poisson's ratios value of 0.23 [33] for pure $ZrO_2$.

Besides the primary load transfer from the Al phase to the $Al_2O_3$ phase, there is also a secondary, though much less significant, load transfer within the ceramic reinforcement occurring from the $ZrO_2$ phase to the $Al_2O_3$ phase. $ZrO_2$ was added because (i) it aids sintering by acting as a grain growth inhibitor, (ii) it decreases residual porosity and (iii) it increases overall toughness of the reinforcement by transformation toughening, microcrack toughening and crack deflection [44–46].

### 4.2. Spatially resolved measurements

Unlike bulk measurements where residual $Al_2O_3$ strains are near-zero, those for the spatially resolved measurements are measurable (~100–150 με), but the stress magnitude (estimated as 40–60 MPa using the bulk Young's modulus of pure alumina) is small compared to the fracture strength of alumina. Fig. 7 shows that load transfer varies with position: it is more pronounced (as visible from the lower stress–strain slope) for position (A) than for position (B), corresponding respectively to a horizontal rod and a single "hairpin" connecting two rods.

As visible in Figs. 1 and 3, a horizontal rod consists of alternating regions of columns and struts. The column regions in the rod consist of material in contact, immediately above and below, with two other perpendicular horizontal rods; this region is thus subjected directly to the uniaxial vertical load. The strut region of the horizontal rod connects two vertical columns, and is surrounded vertically by metallic material. The strut is thus under compressive longitudinal stresses transmitted by the surrounding metal, and it is also subjected to transverse compressive stresses, due to the Poisson's expansion of the neighboring columns subjected to longitudinal compressive stresses. These transverse compressive strains translate into longitudinal tensile strains in the struts, opposite in sign to the compressive longitudinal strains resulting from the metallic phase. Thus, the alumina scaffold can be visualized as vertically aligned "fibers" (or columns, as shown in Fig. 3) connected in two dimensions by short horizontal struts.

During compressive loading, the rod (position A) experiences, on average, compressive longitudinal strains and tensile transverse strains (Fig. 7); however, the stress state is far from uniaxial, since the ratio of the two slopes in Fig. 7 is $202/292 = 0.69$, very much in excess of the Poisson's ratio value of 0.33 [43]. Thus, the magnitude of the transverse tensile strains is much higher than expected if the scaffold was under purely uniaxial compressive stress.

By contrast, position B (the "hairpin" between two columns which is similar to a single strut) exhibits a slope ratio of $329/610 = 0.53$, which is closer to the Poisson's ratio of pure alumina. In fact, this slope ratio is close to that found for the bulk measurement of sample S-Al, which is $242/387 = 0.63$. For position B, both slopes are however smal-

ler than for the bulk measurement, indicating that the "hairpins" are subjected to smaller stresses than the average scaffold. Fracture is thus less likely to occur in the hairpins.

### 4.3. Load transfer modeling by rule-of-mixture

As illustrated in Fig. 8, the complex 3-D architecture of the composites was modeled using a simplified 2-D rule-of-mixture approach [47] leading to three simplified models (labeled ROM-1, ROM-2 and ROM-3), which are similar to those models presented for IPCs in Refs. [10,16,40,41,48–53] and provide the longitudinal and transverse apparent elastic moduli for the $Al_2O_3$ phase, $E_{app,cer}$, corresponding to the experimentally measured slopes of the stress–elastic strain curves in Figs. 4–7. Input parameters are the Young's modulus $E$ and Poisson's ratio $v$ of the metallic phase ($E_{Al} = 69$ GPa and $v_{Al} = 0.33$ [43], $E_{Al7075} = 71.7$ GPa and $v_{Al7075} = 0.33$ [43]) and the ceramic phase ($E_{Al2O3\text{-}ZrO2} = 365$ GPa and $v_{Al2O3\text{-}ZrO2} = 0.26$). The latter parameters are calculated based on the Eshelby method and on simple rule-of-mixtures, respectively, from the moduli and from Poisson's ratios of pure $Al_2O_3$ ($E_{Al2O3} = 380$ GPa and $v_{Al2O3} = 0.26$ [33]) and pure, partially stabilized $ZrO_2$ ($E_{ZrO2} = 205$ GPa and $v_{ZrO2} = 0.23$ [33]). Calculated apparent moduli according to the ROM models are listed in Table 1, assuming a pure Al volume fraction of 50%, as measured experimentally for sample S-Al. This corresponds to a volume fraction $f_1 = 0.5$ for the Al metal phase and a volume fraction $f_2 + f_3 = 0.5$ for the ceramic reinforcement (95% $Al_2O_3$–5% $ZrO_2$), where $f_2 = 0.25$ and $f_3 = 0.25$.

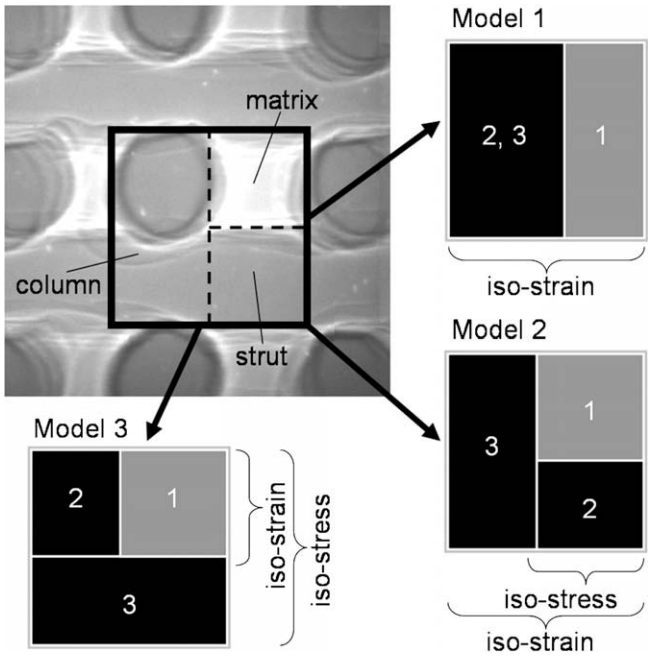


Fig. 8. Rule-of-mixture models for an interpenetrating ceramic–metal composite, with phase 1 for the metal, and phase 2 and 3 for the ceramic. Model ROM-1 assumes iso-strain for both phases. Model ROM-2 considers ceramic within a vertical column (region 3), and a combination of ceramic horizontal struts and metal phase (region 1 + 2). Model ROM-3 considers a combination of metal and ceramic column (regions 1 + 2) and a ceramic rod (region 3, consisting of both column and strut regions).

The models are derived in Appendix A and their geometry is illustrated in Fig. 8. Model ROM-1 is the most simplistic and assumes that all ceramic (in both struts and columns) is present as longitudinal fibers (or slabs) within the metal phase, both phases creating an iso-strain composite. Model ROM-2 considers two regions: (i) ceramic within a vertical column (region 3); and (ii) a mixture of metal phase (region 1) and horizontal ceramic strut (region 2). The latter region (1 + 2) is modeled as an iso-stress composite which is in parallel with the former region 3 forming an iso-strain composite. The total ceramic strain is then obtained by a volume averaging of the strains in the ceramic column (region 3) and strut (region 2). Model ROM-3 also considers two regions: (i) a mixture of metal phase (region 1) and ceramic columns (region 2); and (ii) a mixture of ceramic horizontal strut and ceramic column (region 3). The former region (1 + 2) is modeled as an iso-strain composite which is stacked with the latter region 3 in an iso-stress composite. The total ceramic strain is again obtained by a volume averaging of the strains in the ceramic columns and struts.

### 4.4. Load transfer modeling by finite-element calculations

Calculations are performed using the ABAQUS software package [54]. Three-dimensional finite-element modeling using spatially repeating simple unit cells has been shown to be a powerful method for investigating load sharing between phases in composites [27,55–57]. In the present case, given the 3-D periodic architecture of the composite, a unit-cell approach is particularly appropriate. Although these composites have tetragonal symmetry, they are not significantly far from cubic symmetry, so that cubic symmetry is assumed for simplicity. The model, shown in Fig. 9, consists of a cube containing two ceramic rods stacked perpendicular to each other, with dimensions chosen to achieve a rod volume fraction of 50.0% for S-Al and 56.7% for S-7075. Only one-quarter of each rod is used, as allowed by the use of infinite, periodic boundary conditions

Table 1
Calculated composite modulus $E_c$ and apparent phase moduli $E_{app}$ for each phase (met: metal, cer: ceramic) and each direction (no label: longitudinal, trans: transverse) according to the three ROM and two FE models for a pure Al volume fraction of 50% (as measured experimentally for sample S-Al) and a 95% $Al_2O_3$–5% $ZrO_2$ ceramic fraction of 50%.

| | $E_c$ | $E_{app,met}$ | $E_{app,cer}$ | $E_{app,met,trans}$ | $E_{app,cer,trans}$ |
|---|---|---|---|---|---|
| ROM-1 | 217 | 217 | 217 | −811 | −811 |
| ROM-2 | 162 | 118 | 257 | −359 | −997 |
| ROM-3 | 150 | 126 | 187 | −381 | −530 |
| FE-1 | 160 | 128 | 262 | −863 | −520 |
| FE-2 | 156 | 126 | 253 | −837 | −509 |

All values are in GPa.

with mirror planes, which simulate an infinite cubic-symmetry array of ceramic rods stacked with a regular 0/90° architecture, embedded within a metallic phase. The total number of elements (C3D20) was 9228 for the metal phase and 6368 for the ceramic rods. The lower horizontal plane of the model is constrained in the vertical direction, with one corner fully constrained to prevent overall model translation due to floating-point round-off errors. A vertical compressive force is applied to each node on the upper horizontal plane of the model, simulating a uniform stress. The same metal and ceramic elastic constants were used as for the ROM calculations. The ceramic is assumed to remain elastic, while the metallic phase can deform plastically according to published stress–strain curves for pure aluminum (Al-1100) and the Al 7075 alloy [58], with yield stresses of 33 and 531 MPa, respectively, with the Al 7075 alloy strain-hardening significantly more than pure aluminum. Two finite-element models (FE-1 and FE-2) were cre-

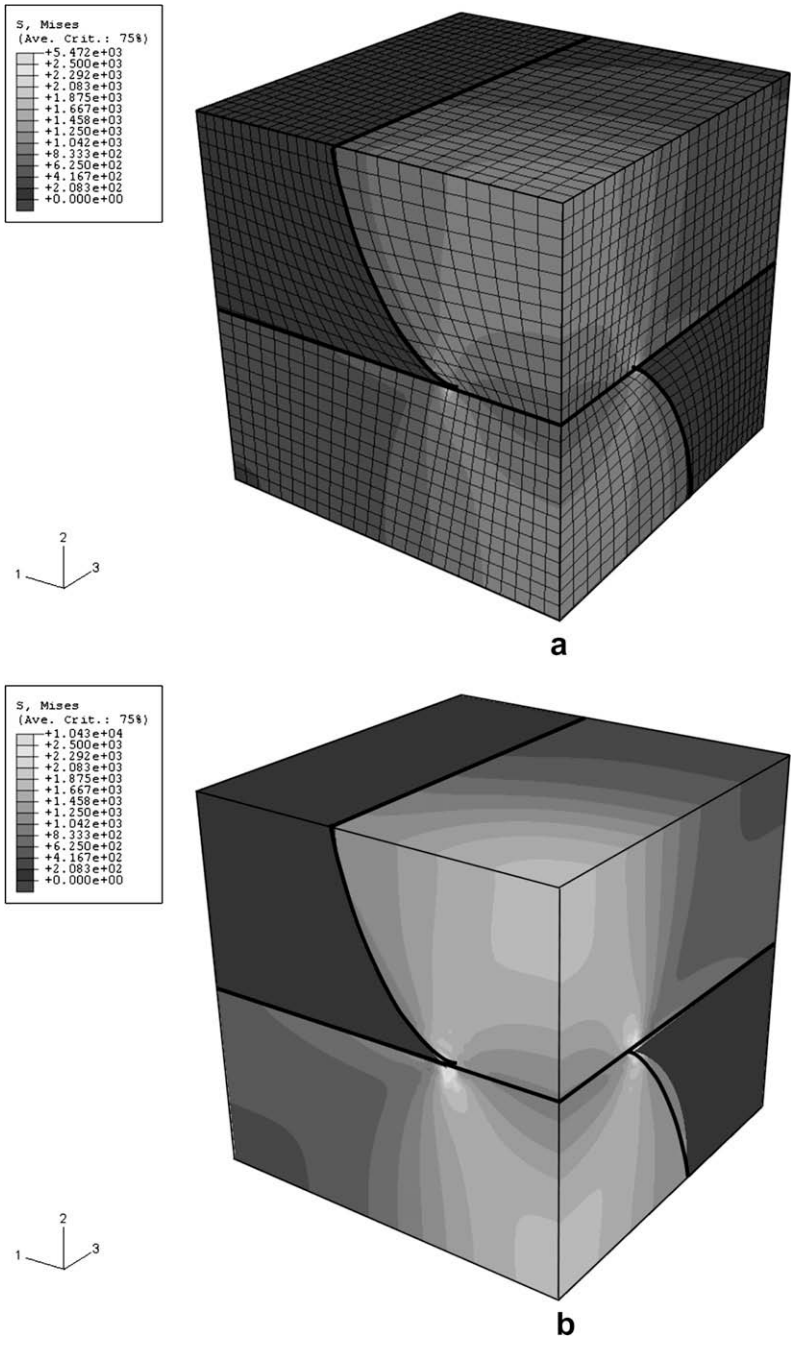


Fig. 9. Finite-element model (FE-2: 95% $Al_2O_3$–5% $ZrO_2$) for a cubic symmetry composite showing the von Mises stress distribution (a) at −210 MPa (with mesh) and (b) at a maximum stress of −360 MPa (without mesh). One quarter rod perpendicular to and stacked upon another quarter rod represents the ceramic reinforcement embedded in a cube of Al metal phase. The thick black lines highlight the two rods.

ated, with ceramic phases consisting of 100% $Al_2O_3$ and 95% $Al_2O_3$–5% $ZrO_2$, respectively.

An example of the von Mises stress distribution using finite-element model FE-2 (95% $Al_2O_3$–5% $ZrO_2$) for a composite with 50.0 vol.% (corresponding to sample S-Al) is shown in Fig. 9 for applied stresses of −210 (the onset of plasticity) and −360 MPa (the maximum stress used experimentally). As illustrated in Fig. 9, non-uniform stress in the ceramic reinforcement, as well as load transfer from the metal to the ceramic phase, are observed. Like the spatially resolved experimental data for the $Al_2O_3$ phase, higher stresses are observed in the ceramic column compared to the ceramic struts. The largest stresses are observed in the center of the rods and at the notch at the contact line between the two ceramic rods; however, there is also a stress reduction at the contact plane away from the contact line, which is likely a Hertzian contact effect.

An example of the longitudinal elastic strain distribution at a maximum applied stress of −360 MPa in the longitudinal and transverse directions is shown in Fig. 10a and b. In the longitudinal direction, the Al plastic zone is limited only to a small fraction of the Al phase at the interface between the Al metal and the $Al_2O_3$ ceramic reinforcement, where the hydrostatic component is larger. In the transverse direction, the Al plastic zone is non-uniformly distributed with higher strain observed in the center of the Al metal and at the interface under the ceramic rods.

### 4.5. Comparison between the ROM and FE models

From Table 1, the modulus of the composite is stiffest in the ROM-1 model ($E_c = 217$ GPa), as expected. The modulus of the composite for the ROM-2 ($E_{C2} = 162$ GPa) and ROM-3 ($E_{C3} = 150$ GPa) models are both approximately three-fourths of that of the ROM-1 model ($E_c = 217$ GPa) and bracket the values of the more realistic FE models ($E_c = 160$ and 156 GPa).

The apparent modulus of the ceramic reinforcement in the longitudinal direction ($E_{app,cer}$) are in the range 190–260 GPa for the ROM-1, ROM-2, and ROM-3 models. The values for ROM-1 (217 GPa) and ROM-3 (187 GPa) models are significantly lower than values predicted by the FE models (253–262 GPa), i.e. FE is predicting that the strain on the ceramic, and thus the load transfer to the ceramic, is less than these simplified ROM models. Only the ROM-2 (257 GPa) model predicts a similar value to the FE models and is thus relatively accurate at predicting the value in the longitudinal direction. However, the apparent modulus of the ceramic reinforcement in the transverse direction ($E_{app,cer,trans}$) for the ROM-1 and ROM-2 (−811 to −997 GPa) predict much larger values than ROM-3 and the two FE models (−500 to −530 GPa). While differences are expected, given how much more simplified the ROM models are as compared to the FE models, it is difficult to determine a priori the magnitude of the difference.

### 4.6. Comparison between the experimental data and the models

As illustrated in Figs. 4a and 6, the apparent $Al_2O_3$ moduli predicted by the ROM and FE models ($E_{app,cer}$) are compared with bulk measurements from $Al_2O_3$ (1 1 3) for the S-Al and S-7075 bulk composite measurement for the longitudinal ($\varepsilon_{11}$) and transverse ($\varepsilon_{22}$) directions. All models assume elastic isotropy, and can thus only give an average response for each of the phases. For each set of data, the appropriate ceramic volume fraction (50.0 vol.% for S-Al and 56.7 vol.% for S-7075) were used for the calculations. The ROM-1 and FE-2 models have values (217 and 253 GPa, respectively) for the apparent ceramic modulus in the longitudinal direction within the range determined experimentally (216–254 GPa), while the ROM-2 (257 GPa) slightly overpredicts the value and the ROM-3 (187 GPa) model significantly underpredicts the value. The FE-1 model (assuming 100% $Al_2O_3$) predicts an apparent modulus (262 GPa) slightly above the upper limit of the experimental range, while the FE-2 model (with a more realistic 95% $Al_2O_3$, 5% $ZrO_2$) is within the experimental range with 253 GPa. All of the models underpredict the strain in the transverse direction and thus overpredict the experimental values (−340 to −430 GPa) for the apparent ceramic modulus in the transverse direction; however, the ROM-3 (−530 GPa), FE-1 (−520 GPa) and FE-2 (−509 GPa) models are much closer to the experimental values observed. This underprediction of the strain in the transverse direction may be a result of the slight deviation from linearity observed in the experimental data, possibly due to damage of the ceramic phase.

Although very simplistic, the ROM-1 model matches reasonably well with the experimental data in the longitudinal direction but drastically underpredicts the experimental strains in the transverse direction. Similar to the ROM-1 model, but with a slightly more realistic geometry, the ROM-2 model only slightly overpredicts the experimental data in the longitudinal direction, but underpredicts even more the strain in the transverse. This is also true with the ROM-3 model, but the ROM-3 model significantly overpredicts the strain in the longitudinal direction; however, this model, while still underpredicting the strain in the transverse direction, matches the experimental data in the transverse direction much better than both the ROM-1 and ROM-2 models. Unlike the ROM models, the two FE models match the experimental data reasonably well in both the longitudinal and transverse directions, but slightly underpredict the strains. All of the models fail to capture the slight deviation from linearity observed in the experimental data at higher stresses, which is possibly a result of damage in the ceramic phase.

A limitation common to both models is that they assume elastic isotropy and can thus only give an average response for each of the phases present. Additionally, the measured data are for a specific $Al_2O_3$ reflection (1 1 3) and the models use the average modulus for the $Al_2O_3$

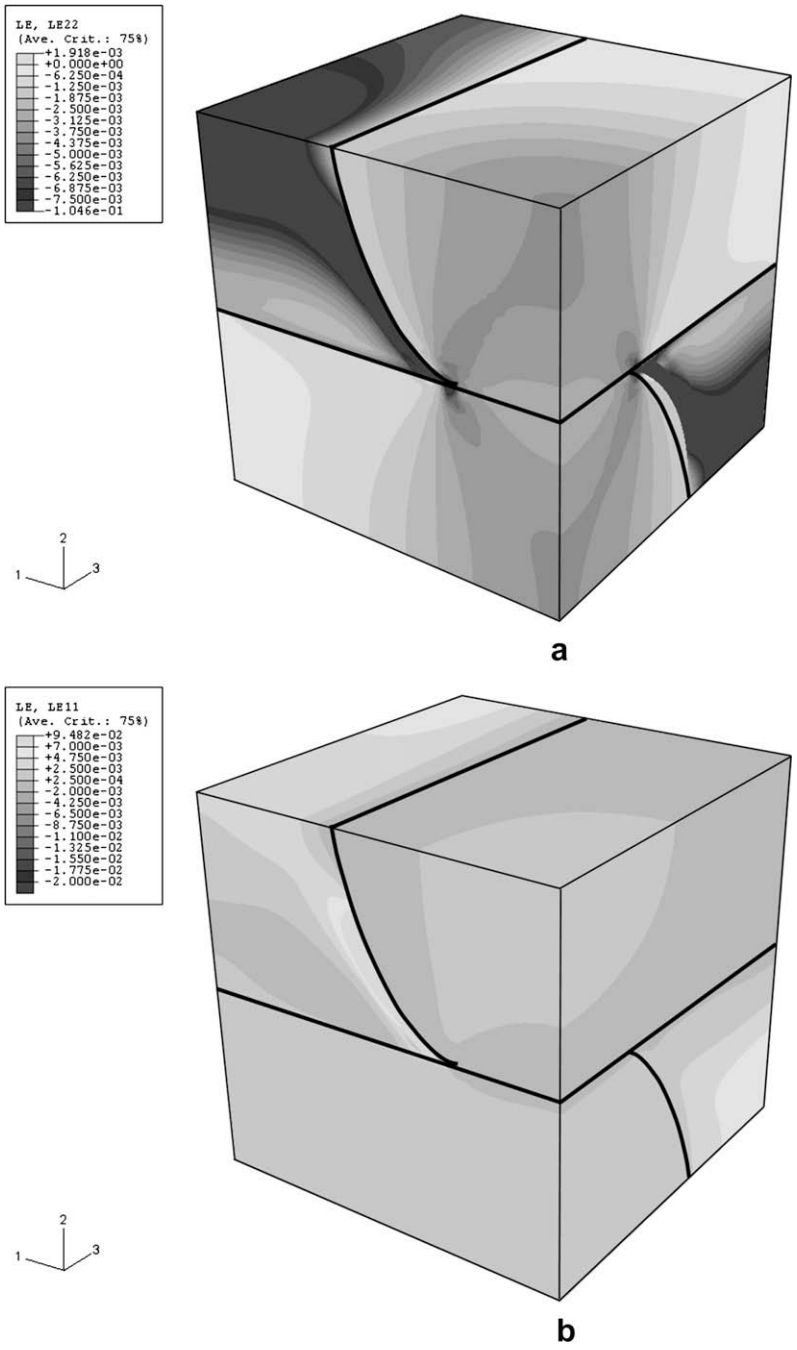


Fig. 10. Finite-element model for a cubic symmetry composite showing the elastic strain distribution at a maximum stress of −360 MPa in (a) the longitudinal direction and (b) the transverse direction. One quarter rod perpendicular to and stacked upon another quarter rod represents the ceramic reinforcement embedded in a cube of Al metal phase. The thick black lines highlight the two rods.

phase. Fortunately, as illustrated in Fig. 5, very little anisotropic effects are present in the $Al_2O_3$ phase. Therefore, some error is associated in both the theoretical value and in the experimental value used for the modulus of the $Al_2O_3$ phase. Another limitation is that the models treat the $Al_2O_3$–5% $ZrO_2$ phase as homogeneous, ignoring its true structure that consists of an $Al_2O_3$ matrix containing particles of $ZrO_2$. Another possible source of error is associated with the facts that the model is perfectly aligned with the applied stress, and that no defects such as cracks, interface delamination or "hairpins" near the edges are considered. Finally, another source of error is that the models treat the metal "skin" as additional metal phase and do not account for the edge effects that may occur with a pure metal "skin". These edge effects weaken the overall composite and are expected to lower the overall amount of strain observed in the ceramic phase. None of the models considers the possibility of fracture in the ceramic, which may explain the discrepancy in the longitudinal and transverse directions, especially for the FE models.

A specific limitation of the ROM models is that they are not 3-D models and so treat the phases as 2-D slabs, which are a poor representation of the complex geometry of the composites. Finite-element modeling overall is an improvement over the ROM models since it is more complex and matches more closely with the experimental geometry at the global level (struts, columns, and rods) and at the local level (curved region and then flat surface at contact between rods). Furthermore, the finite element provides physical continuity between the phases at all interfaces and takes into account metal plasticity, unlike the ROM models.

## 5. Conclusions

Interpenetrating $Al_2O_3$–Al composites are produced by liquid-metal infiltration of 3-D periodic $Al_2O_3$ preforms fabricated by direct-write assembly, and subjected to synchrotron X-ray diffraction to measure elastic strains in the ceramic phase. The as-fabricated composites exhibit low residual strains in the ceramic phase from thermal mismatch. During uniaxial compression, longitudinal ceramic strains increase linearly with applied stress, despite the onset of metal plasticity and possible damage accumulation in the ceramic. The high values of these strains indicate that load transfer is occurring from the metallic phase. Simple rule-of-mixture models (assuming purely elastic behavior) and more complex finite-element models (allowing for metal plasticity and taking into account the complex geometry of the composites) can predict with reasonable accuracy the strains in the ceramic phase. Spatially resolved measurements show that more strain (and thus higher stress) is observed in the horizontal ceramic "rods" than in the ceramic "hairpin" connecting them, as expected.

## Acknowledgements

The authors thank the following APS researchers for experimental assistance: Drs. Ulrich Lienert, Kamel Fezzaa, and Wah-Keat Lee (SRI-CAT) and Dr. Mark Beno and Chuck Kurtz (BESSRC-CAT). Use of the APS was supported by the U.S. Department of Energy, Office of Science, Office of Basic Energy Science, under contract number DE-AC02-06CH11357. J.A.L. and R.R. acknowledge funding provided by NSF Grant # (DMR01-17792).

## Appendix A. Model ROM-1

The first model assumes that all ceramic (in both struts and columns) is present as longitudinal slabs (or fibers) within the metal phase, from which a longitudinal iso-strain composite modulus and the strain in the ceramic phase are calculated using the following equations:

$$\varepsilon_{C1} = \varepsilon_1 = \varepsilon_{2,3} = \frac{\sigma_{app}}{E_{C1}} \tag{1}$$

where $\varepsilon_{C1}$ is the longitudinal strain in the composite, $\varepsilon_1$ is the longitudinal strain in the metal, $\varepsilon_{2,3}$ is the longitudinal strain in the ceramic reinforcement, $\sigma_{app}$ is the applied stress and $E_{C1}$ is the Young's modulus of the composite for Model 1, given by the rule-of-mixture (ROM):

$$E_{C1} = f_1 E_{met} + (f_2 + f_3) E_{cer} \tag{2}$$

where $E_{met}$ is the Young's modulus of the metal, $E_{cer}$ is the Young's modulus of the ceramic reinforcement, $f_1$ is the volume fraction of the metal phase, and $f_2$ and $f_3$ are the two components of the volume fraction of the ceramic reinforcement.$E_{C1,app,,trans}$, the apparent modulus of the composite in the transverse direction for Model 1, is defined as:

$$E_{C1,app,trans} = \frac{f_1 E_{met}}{-\nu_{met}} + \frac{(f_2 + f_3) E_{cer}}{-\nu_{cer}} \tag{3}$$

## Appendix B. Model ROM-2

### B.1. Longitudinal direction

The second model considers two regions: (i) ceramic within a vertical column (region 3); and (ii) a combination of ceramic horizontal struts and metal (region $1 + 2$). The latter region is modeled as an iso-stress sub-composite which is combined in parallel with the former region in an iso-strain composite. The overall ceramic strain is then obtained by a volume averaging of the strains in the ceramic columns (region 3) and struts (region 2). We start from the following iso-stress equation for region $1 + 2$:

$$\sigma_1 = \sigma_2 = \varepsilon_1 E_{met} = \varepsilon_2 E_{cer} = \varepsilon_{1,2} E_{1,2} \tag{4}$$

where $\sigma_1$ is the applied stress in the metal phase, $\sigma_2$ is the applied stress in the horizontal strut, $\varepsilon_1$ is the longitudinal strain in the metal phase, $\varepsilon_2$ is the longitudinal strain in the horizontal strut, $E_{1,2}$ is the Young's modulus of the iso-stress component and $\varepsilon_{1,2}$ is the longitudinal strain in the iso-stress component, which is then used in the following iso-strain equation to solve for $E_{C2}$:

$$\varepsilon_{C2} = \varepsilon_3 = \varepsilon_{1,2} = \frac{\sigma_{app}}{E_{C2}} \tag{5}$$

In this second model, $E_{C2}$ (the modulus of the composite) is given by the ROM as:

$$E_{C2} = (f_1 + f_2) E_{1,2} + f_3 E_{cer} \tag{6}$$

where $E_{1,2}$ is given by the ROM as:

$$E_{1,2} = \left( \frac{\frac{f_1}{f_1+f_2}}{E_{met}} + \frac{\frac{f_2}{f_1+f_2}}{E_{cer}} \right)^{-1} = (f_1 + f_2) \left( \frac{f_1}{E_{met}} + \frac{f_2}{E_{cer}} \right)^{-1} \tag{7}$$

From these equations, the apparent modulus (slope of the applied stress vs. elastic strain plots) of the metal phase $E_{app,met}$ can be found from the following equations,

Starting with:

$$E_{app,met} = \frac{\sigma_{app}}{\varepsilon_1} \tag{8}$$

and using the iso-stress relations for $\varepsilon_1$ from Eq. (4) and the iso-strain relations for $\varepsilon_{1,2}$ from Eq. (5), a compact form for $E_{app,met}$ is found to be:

$$E_{app,met} = \frac{E_{C2}E_{met}}{E_{1,2}} \tag{9}$$

Substituting Eqs. (6) and (7) into Eq. (9), this equation can be put into terms of the Young's moduli of the metal ($E_{met}$) and the ceramic ($E_{cer}$), as well as the volume fractions ($f_1$, $f_2$ and $f_3$) of the metal and the ceramic phases, as follows:

$$E_{app,met} = \frac{\left((f_1+f_2)^2\left(\frac{f_1}{E_{met}}+\frac{f_2}{E_{cer}}\right)^{-1}+f_3E_{cer}\right)E_{met}}{(f_1+f_2)\left(\frac{f_1}{E_{met}}+\frac{f_2}{E_{cer}}\right)^{-1}} \tag{10}$$

The apparent modulus of the ceramic reinforcement $E_{app,cer}$ is found by starting with:

$$E_{app,cer} = \frac{\sigma_{app}}{\varepsilon_{2,3}} \tag{11}$$

where $\varepsilon_{2,3}$, the longitudinal average strain in the ceramic reinforcement, is obtained by volume averaging the strains in the ceramic columns (region 3) and struts (region 2):

$$\varepsilon_{2,3} = \frac{f_2\varepsilon_2+f_3\varepsilon_3}{f_2+f_3} \tag{12}$$

Using the iso-stress relations for $\varepsilon_2$ from Eq. (4) and the iso-strain relations for $\varepsilon_{1,2}$ and $\varepsilon_3$, Eq. (11) becomes:

$$E_{app,cer} = (f_2+f_3)\left(\frac{E_{C2}E_{cer}}{f_2E_{1,2}+f_3E_{cer}}\right) \tag{13}$$

which can be expressed in terms of $E_{met}$, $E_{cer}$ and the volume fractions ($f_1$, $f_2$ and $f_3$) as:

$$E_{app,cer} = (f_2+f_3)\left(\frac{\left((f_1+f_2)^2\left(\frac{f_1}{E_{met}}+\frac{f_2}{E_{cer}}\right)^{-1}+f_3E_{cer}\right)E_{cer}}{f_2(f_1+f_2)\left(\frac{f_1}{E_{met}}+\frac{f_2}{E_{cer}}\right)^{-1}+f_3E_{cer}}\right) \tag{14}$$

### B.2. Transverse direction

To find the modulus of the composite and the apparent moduli of the metal and ceramic phases in the transverse direction, the Poisson's ratio of the metal and ceramic phases, $\nu_{met}$ and $\nu_{cer}$, are used. The apparent transverse modulus of the metal is defined as:

$$E_{app,met,trans} = \frac{\sigma_{app}}{\varepsilon_{1,trans}} = \frac{\sigma_{app}}{-\nu_1\varepsilon_1} = \frac{\sigma_{app}E_{met}}{-\nu_1\varepsilon_{1,2}E_{1,2}} \tag{15}$$

where the transverse strains $\varepsilon_1$ and $\varepsilon_{1,2}$ are given by the iso-strain relations from Eq. (5), leading to the following equation:

$$E_{app,met,trans} = \frac{-E_{C2}E_{met}}{\nu_1E_{1,2}} \tag{16}$$

Introducing $E_{1,2}$ and $E_{C2}$ as given by the ROM in Eqs. (6) and (7) gives:

$$E_{app,met,trans} = -\left(f_1+f_2+\frac{f_3E_{cer}}{(f_1+f_2)\left(\frac{f_1}{E_{met}}+\frac{f_2}{E_{cer}}\right)^{-1}}\right)\frac{E_{met}}{\nu_{met}} \tag{17}$$

Similarly, the apparent transverse modulus of the ceramic is defined as:

$$E_{app,cer,trans} = \frac{\sigma_{app}}{\varepsilon_{2,3,trans}} \tag{18}$$

where $\varepsilon_{2,3,trans}$, as in Eq. (12), is obtained by volume averaging the transverse strains in the ceramic columns (region 3) and struts (region 2):

$$\varepsilon_{2,3,trans} = \frac{f_2\varepsilon_{2,trans}+f_3\varepsilon_{3,trans}}{f_2+f_3} \tag{19}$$

and the transverse strains $\varepsilon_{2,trans}$ and $\varepsilon_{3,trans}$ are defined as:

$$\varepsilon_{2,trans} = -\nu_2\varepsilon_2 \tag{20a}$$

$$\varepsilon_{3,trans} = -\nu_3\varepsilon_3 \tag{20b}$$

where the longitudinal strains $\varepsilon_2$ and $\varepsilon_3$ are defined by the iso-stress and iso-strain relations in Eq. (4) and (5), respectively. Then, $E_{app,cer,trans}$ becomes:

$$E_{app,cer,trans} = -\left(\frac{(f_2+f_3)((f_1+f_2)E_{1,2}+f_3E_{cer})}{f_2E_{1,2}+f_3E_{cer}}\right)\frac{E_{cer}}{\nu_{cer}} \tag{21}$$

## Appendix C. Model ROM-3

### C.1. Longitudinal direction

Like the second model (ROM-2), this model considers two regions: (i) a mixture of ceramic columns and metal phase (region 1 + 2); and (ii) a mixture of ceramic horizontal struts and ceramic columns (region 3). The former region (1 + 2) is modeled as an iso-strain sub-composite which is combined in series with the latter region 3 in an iso-stress composite. The total ceramic strain is again obtained by a volume averaging of the strains in the ceramic columns and struts using the following iso-strain equation:

$$\varepsilon_{1,2} = \varepsilon_1 = \varepsilon_2 = \frac{\sigma_{1,2}}{E_{1,2}} = \frac{\sigma_1}{E_{met}} = \frac{\sigma_2}{E_{cer}} \tag{22}$$

where $\varepsilon_{1,2}$ is the longitudinal strain in the iso-strain component, $\varepsilon_1$ is the longitudinal strain in the metal phase, $\varepsilon_2$ is the longitudinal strain in part of the ceramic columns, $\sigma_{1,2}$ is the applied stress of the iso-strain component, and $E_{1,2}$ is the Young's modulus of the iso-strain component, which is defined as:

$$E_{1,2} = f_1E_{met}+f_2E_{cer} \tag{23}$$

The Young's modulus of the iso-strain component ($E_{1,2}$) can be related to region 3 by the following iso-stress equation:

$$\sigma_{1,2} = \sigma_3 = \sigma_{app} = \varepsilon_3 E_{cer} = \varepsilon_{1,2} E_{1,2} = \varepsilon_{C3} E_{C3} \tag{24}$$

where $\sigma_{1,2}$ is the applied stress in the iso-strain component, $\sigma_3$ is the applied stress in region 3 and $\varepsilon_3$ is the longitudinal strain in region 3. The modulus of the composite ($E_{C3}$) is given by the ROM as:

$$E_{C3} = \left(\frac{f_1 + f_2}{E_{1,2}} + \frac{f_3}{E_{cer}}\right)^{-1} \tag{25}$$

and substituting Eq. (23) into Eq. (25) gives:

$$E_{C3} = \left(\frac{f_1 + f_2}{f_1 E_{met} + f_2 E_{cer}} + \frac{f_3}{E_{cer}}\right)^{-1} \tag{26}$$

From these equations, the apparent modulus of the metal phase can be solved from the following equation:

$$E_{app,met} = \frac{\sigma_{app}}{\varepsilon_1} \tag{27}$$

and introducing Eq. (22) into Eq. (27) gives:

$$E_{app,met} = E_{1,2} \tag{28}$$

From Eq. (23), Eq. (28) is the same as:

$$E_{app,met} = f_1 E_{met} + f_2 E_{cer} \tag{29}$$

Now, the apparent modulus of the ceramic phase can be solved accordingly:

$$E_{app,cer} = \frac{\sigma_{app}}{\varepsilon_{2,3}} \tag{30}$$

where $\varepsilon_{2,3}$, the average longitudinal strain of the ceramic phase, like Eq. (12), is defined as:

$$\varepsilon_{2,3} = \left(\frac{f_2 \varepsilon_2 + f_3 \varepsilon_3}{f_2 + f_3}\right) \tag{31}$$

Substituting this equation into Eq. (30) gives:

$$E_{app,cer} = \frac{\sigma_{app}}{\frac{f_2 \varepsilon_2 + f_3 \varepsilon_3}{f_2 + f_3}} \tag{32}$$

and by using the iso-strain relations for $\varepsilon_2$ from Eq. (22), for $\varepsilon_3$ from Eq. (24) and the iso-stress relations for $\varepsilon_{1,2}$ and $\varepsilon_3$ from Eq. (25), ceramic apparent modulus becomes:

$$E_{app,cer} = \frac{\sigma_{app}(f_2 + f_3)}{\frac{f_2 \sigma_{app}}{E_{1,2}} + \frac{f_3 \sigma_{app}}{E_{cer}}} \tag{33}$$

which further simplifies, using Eq. (23), to:

$$E_{app,cer} = \frac{f_2 + f_3}{\frac{f_2}{f_1 E_{met} + f_2 E_{cer}} + \frac{f_3}{E_{cer}}} \tag{34}$$

### C.2. Transverse direction

Poisson's ratio is used, similar to Eq. (15), to find the apparent transverse modulus of the metal phase as:

$$E_{app,met,trans} = \frac{\sigma_{app}}{\varepsilon_{1,trans}} = \frac{\sigma_{app}}{-\nu_1 \varepsilon_1} = \frac{-E_{1,2}}{\nu_1} \tag{35}$$

where $\varepsilon_1$ is given by the iso-stress relations from Eq. (22) and $E_{1,2}$ is given by the ROM in Eq. (23), leading to:

$$E_{app,met,trans} = \frac{f_1 E_{met} + f_2 E_{cer}}{-\nu_{met}} \tag{36}$$

Using Eq. (18), the apparent transverse modulus of the ceramic phase is defined as:

$$E_{app,cer,trans} = \frac{\sigma_{app}}{\varepsilon_{2,3,trans}} \tag{37}$$

where $\varepsilon_{2,3,trans}$, like Eq. (12) and (19), is obtained by volume averaging the transverse strains in the ceramic columns (region 3) and struts (region 2) as:

$$\varepsilon_{2,3,trans} = \frac{f_2 \varepsilon_{2,trans} + f_3 \varepsilon_{3,trans}}{f_2 + f_3} \tag{38}$$

As for Eq. (20a,b), the transverse strains $\varepsilon_{2,trans}$ and $\varepsilon_{3,trans}$ are defined as follows:

$$\varepsilon_{2,trans} = -\nu_2 \varepsilon_2 \tag{20a}$$

$$\varepsilon_{3,trans} = -\nu_3 \varepsilon_3 \tag{20b}$$

where $\varepsilon_2$ and $\varepsilon_3$ are given by the iso-strain and iso-stress relations in Eqs. (22) and (24), respectively. Then, $E_{app,cer,trans}$ *becomes:*

$$E_{app,cer,trans} = \frac{-(f_2 + f_3)(f_1 E_{met} + f_2 E_{cer}) E_{C3}}{f_2 \nu_{cer} E_{C3} + f_3 \nu_{cer}(f_1 E_{met} + f_2 E_{cer})} \tag{39}$$

## References


[1] Clarke DR. J Am Ceram Soc 1992;75:739.
[2] Prielipp H, Knechtel M, Claussen N, Streiffer SK, Mullejans H, Ruhle M, et al. Mater Sci Eng A 1995;197:19.
[3] Skirl S, Hoffman M, Bowman K, Wiederhorn S, Rodel J. Acta Mater 1998;46:2493.
[4] Zimmermann A, Hoffman M, Emmel T, Gross D, Rodel J. Acta Mater 2001;49:3177.
[5] Kouzeli M, Dunand DC. Acta Mater 2003;51:6105.
[6] Kouzeli M, Dunand DC. Metall Mater Trans A 2004;35A:287.
[7] Ewsuk KG, Glass SJ, Loehman RE, Tomsia AP, Fahrenholtz WG. Metall Mater Trans A 1996;27:2122.
[8] Loehman RE, Ewsuk KG, Tomsia AP. J Am Ceram Soc 1996;79:27.
[9] Breslin MC, Ringnalda J, Xu L, Fuller M, Seeger J, Daehn GS, et al. Mater Sci Eng A 1995;195:113.
[10] Liu W, Koester U. Mater Sci Eng A 1996;210:1.
[11] San Marchi C, Kouzeli M, Rao R, Lewis JA, Dunand DC. Scripta Mater 2003;49:861.
[12] Cesarano J, Calvert P. US Patent 6 027 326. US; 2000.
[13] Smay JE, Cesarano J, Lewis JA. Langmuir 2002;18:5429.
[14] Smay JE, Gratson GM, Shepherd RF, Cesarano J, Lewis JA. Adv Mater 2002;14:1279.
[15] Seerden KAM, Reis N, Evans JRG, Grant PS, Halloran JW, Derby B. J Am Ceram Soc 2001;84:2514.
[16] Morissette SL, Lewis JA, Clem PG, Cesarano J, Dimos DB. J Am Ceram Soc 2001;84:2462.
[17] Bandyopadhyay A, Das K, Marusich J, Onagoruwa S. Rapid Prototyping J 2006;12:121.
[18] Soundararajan R, Kuhn G, Atisivan R, Bose S, Bandyopadhyay A. J Am Ceram Soc 2001;84:509.

[19] Young ML, Almer JD, Lienert U, Haeffner DR, Rao R, Lewis JA, et al. In: Pandey AB, Kendig KL, Lewandowski JJ, Shah SR, editors. MS&T conference proceedings: affordable metal matrix composites for high performance applications II. Mater Sci Tech Ser. Chicago, IL; 2003. p. 225.
[20] Mortensen A. Comprehensive composite materials. New York: Elsevier; 2000.
[21] Balch DK, Ustundag E, Dunand DC. Metall Mater Trans A 2003;34A:1787.
[22] Wanner A, Dunand DC. Metall Mater Trans A 2000;31:2949.
[23] Almer JD, Stock SR. J Struct Biol 2005;152:14.
[24] Balch DK, Dunand DC. Acta Mater 2006;54:1501.
[25] Haeffner DR, Almer JD, Lienert U. Mater Sci Eng A 2005;399:120.
[26] Wanner A, Dunand DC. J Neutron Res 2002;10:57.
[27] Young ML, Almer JD, Daymond MR, Haeffner DR, Dunand DC. Acta Mater 2007;55:1999.
[28] Young ML, DeFouw JD, Almer JD, Haeffner DR, Dunand DC. Acta Mater 2007;55:3467.
[29] Hammersley AP. ESRF97HA02T, FIT2D: an introduction and overview. ESRF internal report; 1997.
[30] Hammersley AP. ESRF98HA01T, FIT2D V9.129 reference manual V3.1. ESRF internal report; 1998.
[31] MATLAB Mathworks. Available from: www.mathworks.com.
[32] Balch DK, Ustundag E, Dunand DC. J Non-Cryst Solids 2003;317:176.
[33] Engineering materials handbook, vol. 4. Ceramics and glasses. Metals Park, OH: ASM International; 1991.
[34] Alcoa. Alcoa aluminum handbook. Pittsburgh, PA: Aluminum Company of America; 1962.
[35] Munro RG. J Am Ceram Soc 1997;80:1919.
[36] Dunand DC, Mari D, Bourke MAM, Roberts JA. Metall Mater Trans A 1996;27:2820.
[37] Allen AJ, Bourke MAM, Dawes S, Hutchings MT, Withers PJ. Acta Metall Mater 1992;40:2361.
[38] Wilkes TE, Young ML, Sepulveda RE, Dunand DC, Faber KT. Scripta Mater 2006;55:1083.
[39] Mortensen A, Michaud VJ, Flemings MC. J Miner Met Mater Soc 1993;45:36.
[40] Wegner LD, Gibson LJ. Int J Mech Sci 2000;42:925.
[41] Wegner LD, Gibson LJ. Int J Mech Sci 2000;42:943.
[42] Wegner LD, Gibson LJ. Int J Mech Sci 2001;43:1061.
[43] Metals handbook, vol. 2. Metals Park, OH: ASM International; 1990.
[44] Claussen N. J Am Ceram Soc 1976;59:49.
[45] Evans AG, Cannon RM. Acta Metall 1986;34:761.
[46] Wang J, Stevens R. J Mater Sci 1987;23:804.
[47] Courtney TH. Mechanical behavior of materials. New York: McGraw Hill; 2000.
[48] Tuchinskii LI. Powder Metall Met Ceram 1983;22:588.
[49] Tuchinskii LI, Kalimova NL. Powder Metall Met Ceram 1995;33:314.
[50] Aghajanian MK, MacMillan NH, Kennedy CR, Luszcz SJ, Roy R. J Mater Sci 1989;24:658.
[51] Daehn GS, Starck B, Xu L, Elfishawy KF, Ringnalda J, Fraser HL. Acta Mater 1996;44:249.
[52] Wang JC. J Mater Sci 1984;19:809.
[53] Wang JC. J Mater Sci 1984;19:801.
[54] ABAQUS users manual. Version 6.4. Rhode Island, NY: HKS; 2003.
[55] Gonzalez C, Llorca J. Acta Mater 2001;49:3505.
[56] Livescu V, Clausen B, Paggett JW, Krawitz AD, Drake EF, Bourke MAM. Mater Sci Eng A 2005;399:134.
[57] Shen H, Lissenden CJ. Mater Sci Eng A 2002;338:271.
[58] Boyer HE. Atlas of stress–strain curves. Materials Park, OH: ASM International; 2002.